

Identifying the most crucial parameters of the initial curvature profile for primordial black hole formation

Tomohiro Nakama,^{1,2} Tomohiro Harada,³ A. G. Polnarev,⁴ and Jun'ichi Yokoyama^{2,5}

¹*Department of Physics, Graduate School of Science,
The University of Tokyo, Bunkyo-ku, Tokyo 113-0033, Japan*

²*Research Center for the Early Universe (RESCEU),
Graduate School of Science, The University of Tokyo,
Bunkyo-ku, Tokyo 113-0033, Japan*

³*Department of Physics, Rikkyo University, Toshima, Tokyo 175-8501, Japan*

⁴*Astronomy Unit, School of Physics and Astronomy,
Queen Mary University of London,
Mile End Road, London E1 4NS, United Kingdom*

⁵*Kavli Institute for the Physics and Mathematics of the Universe (Kavli IPMU), WPI, TODIAS,
The University of Tokyo, Kashiwa, Chiba 277-8568, Japan*

(Dated: July 12, 2018)

Abstract

Primordial black holes (PBHs) are an important tool in cosmology to probe the primordial spectrum of small-scale curvature perturbations that reenter the cosmological horizon during radiation domination epoch. We numerically solve the evolution of spherically symmetric highly perturbed configurations to clarify the criteria of PBHs formation using an extremely wide class of curvature profiles characterized by five parameters, (in contrast to only two parameters used in all previous papers) which specify the curvature profiles not only at the central region but also at the outer boundary of configurations. It is shown that formation or non-formation of PBHs is determined essentially by only two master parameters one of which can be presented as an integral of curvature over initial configurations and the other is presented in terms of the position of the boundary and the edge of the core.

PACS numbers:

I. INTRODUCTION

It is well known that a region with large amplitude curvature profile can collapse to a primordial black hole (PBH) [1, 2]. The probability of existence of such regions and hence the abundance of PBHs depends on the physical conditions in the very early universe. PBHs are formed soon after the region enters the cosmological horizon during the radiation-dominated epoch. Even if the contribution of the energy density of PBHs to the total cosmic energy density is extremely small at formation, it drastically increases in the course of subsequent cosmic expansion during radiation domination. For this reason PBHs can be used as a unique and powerful tool for the exploration of very small-scale structure of the early universe. This tool is really unique since there are no alternative techniques to study this small-scale structure.

PBHs with different masses have different cosmological and astrophysical implications. The PBHs with mass smaller than $\sim 10^{15}$ g are especially interesting because by now they would have evaporated through Hawking radiation [3] and their abundance is constrained by the effects of emitted high-energy particles and photons on the Big-Bang Nucleosynthesis [4–9], the gamma-ray background [10–12], galactic and extragalactic antiprotons [13] as well as on the cosmic microwave background radiation (CMB).

PBHs with larger masses would still be present and are constrained by dynamical and lensing effects [14] and by the stochastic gravitational wave background [15, 16]. All these constraints are updated and summarized in [17]. For the mass range between 6×10^{20} g and 4×10^{24} g the most stringent constraint is given by the cosmic dark matter density [18].

Even if PBHs would never have been detected these constraints (being reformulated in terms of the constraints on the amplitude of small-scale perturbations) will provide valuable information on inflationary cosmological models [19–22], which predict formation of super-horizon curvature perturbations [23–26]. So far their large-scale components have been precisely tested by observations of CMB [27, 28] and large-scale structure. It is important to probe the perturbation spectrum on significantly smaller scales as well in order to obtain more helpful information to single out the correct inflation model. Indeed there exist a number of inflation models that predict features at some small scales [29–42] which may lead to PBHs abundances not compatible with observational constraints. So we can gain insights into primordial perturbations on small scales even from the absence of observed PBHs. Or if PHBs are detected in the future it will extend our insight into inflationary models drastically.

In order to consistently use PBHs as a cosmological tool to probe the spectrum of small-scale curvature perturbations, the relation between their mass function and the primordial perturbation spectrum must be clarified. This enterprise involves several steps. First we must clarify the formation condition of PBHs as a functional of the primordial curvature profiles of perturbed regions. Second we must calculate the resultant mass of a PBH for each given profile. Finally we must calculate the probability distribution functional of curvature perturbation spectrum which gives realization probability of curvature profiles leading to PBH formation. This paper is predominantly devoted to the first issue and touches the second one in a preliminary manner. We will consider the second issue in more detail in another paper.

Originally the problem of PBH formation was studied analytically by considering the balance between gravity and pressure gradient which hampers contraction, yielding a simple analytic criterion of PBH formation [43, 44]

$$\frac{1}{3} \lesssim \bar{\delta}_{\text{hc}}, \quad (1.1)$$

where $\bar{\delta}_{\text{hc}}$ is the energy density perturbation averaged over the overdense region evaluated at the time of horizon crossing. This criterion has long been used in papers on theoretical prediction of PBH abundance (but has recently been refined in [60]). In this simple picture, since $\bar{\delta}_{\text{hc}}$ is the density perturbation averaged over the overdense region, the dependence on the profile or shape of perturbed regions has not been taken into account.

However, recent numerical analyses have shown that the condition for PBH formation does depend on the profile of perturbation [45, 46] (see also [47, 48]). Both [45] and [46] used two-parameter families of the initial profile (one corresponding to the amplitude of overdensity and the other to the width of the transition region) and obtained two parametric conditions of PBH formation. It was clear from the above publications that one parametric description was not sufficient. However it was not clear whether the two-parametric description is good enough (say, in comparison with three-parametric description). In the present paper, we extend these preceding analyses by making much more numerical computations of PBH formation based on the initial curvature profile including many more parameters, adopting the five-parameter family of profiles. We show that the criterion of PBH formation can still be expressed in terms of two crucial (master) parameters which represent the averaged amplitude of over density in the central region and the width of transition region at outer boundary, even though the considered profiles belong to the five-parametric family. Thereby we have obtained extra evidence that the two-parametric description mentioned above is self-consistent and provided a reliable physical interpretation of the criterion we have obtained.

In our previous paper [49] (hereafter PNY), we investigated the time evolution of spherical perturbed regions embedded in a flat Friedmann-Lemaitre-Robertson-Walker (FLRW) universe while the region is outside the cosmological horizon, using an asymptotic expansion. In order to calculate the growth of the perturbed region after the horizon reentry, the Einstein equations need to be solved numerically. In this paper, we first present the results of the numerical computation in the slicing used in our previous work, with the initial data generated using the asymptotic expansion. In this slicing, at spatial infinity the time coordinate coincides with that in the background FLRW universe, so this slicing is sometimes referred to as cosmic time slicing in the literature.

During the numerical computation a singularity appears at the centre after the apparent horizon is formed and as a result the computation has to be stopped and the subsequent accretion onto the PBH cannot be followed. That is, the eventual mass of the PBH cannot be obtained. In order to avoid this problem, we employ what is called the null slicing, which is also discussed in this paper.

Finally, note that PBHs are formed only from extremely high peaks of perturbation, corresponding to the tail of the probability distribution of primordial perturbation. The shape of these peaks has been calculated (see, for example, [50, 51]) and has turned out to be nearly spherically symmetric and monotonic near the peak. So in this paper we continue to consider only the spherically symmetric profiles which are monotonic near the centre.

The rest of the paper is organized as follows. In §II, we briefly discuss the initial condition in terms of the asymptotic expansion of the Einstein equations. In §III we present the basic equations used in the numerical computations. Then in §IV we review the time evolution of the perturbation in the cosmic time slicing. In §V we present the two parameters crucial for PBH formation. §VI is devoted to the determination of the PBH masses using the null slicing and §VII to conclusion and discussion.

II. SETTING UP THE INITIAL CONDITION

Assuming spherical symmetry, it is convenient to divide the collapsing matter into a system of concentric spherical shells and to label each shell with a Lagrangian comoving radial coordinate r . Then the metric can be written in the form used by Misner and Sharp [52]:

$$ds^2 = -a^2 dt^2 + b^2 dr^2 + R^2(d\theta^2 + \sin^2 \theta d\phi^2), \quad (2.1)$$

where R , a and b are functions of r and the time coordinate t . We consider a perfect fluid with the energy density $\rho(r, t)$ and pressure $P(r, t)$ and a constant equation-of-state parameter γ , $P(r, t) = \gamma\rho(r, t)$. We express the proper time derivative of R as

$$U \equiv \frac{\dot{R}}{a}, \quad (2.2)$$

with a dot denoting a derivative with respect to t .

We define the mass, sometimes referred to as the Misner-Sharp mass in the literature, within the shell of circumferential radius R by

$$M(r, t) = 4\pi \int_0^{R(r, t)} \rho(r, t) R^2 dR. \quad (2.3)$$

We consider the evolution of a perturbed region embedded in a flat Friedmann-Lemaitre-Robertson-Walker (FLRW) Universe with metric

$$ds^2 = -dt^2 + S^2(t)(dr^2 + r^2 d\theta^2 + r^2 \sin^2 \theta d\phi), \quad (2.4)$$

which is a particular case of (2.1). The scale factor in this background evolves as

$$S(t) = \left(\frac{t}{t_i}\right)^\alpha, \quad \alpha \equiv \frac{2}{3(1+\gamma)}, \quad (2.5)$$

where t_i is some reference time.

We denote the background solution with a suffix 0. In terms of the metric variables defined in (2.1), we find

$$a_0 = 1, \quad b_0 = S(t), \quad R_0 = rS(t). \quad (2.6)$$

The background Hubble parameter is

$$H_0(t) = \frac{\dot{R}_0}{a_0 R_0} = \frac{\dot{S}}{S} = \frac{\alpha}{t}, \quad (2.7)$$

and the energy density is calculated from the Friedmann equation,

$$\rho_0(t) = \frac{3\alpha^2}{8\pi G t^2}. \quad (2.8)$$

The energy density perturbation is defined as

$$\delta(t, r) \equiv \frac{\rho(t, r) - \rho_0(t)}{\rho_0(t)}. \quad (2.9)$$

We introduce a variable H defined by

$$H(t, r) \equiv \frac{\dot{R}}{aR} = \frac{U}{R}. \quad (2.10)$$

The curvature profile $K(t, r)$ is defined by rewriting b as

$$b(t, r) = \frac{R'(t, r)}{\sqrt{1 - K(t, r)r^2}}. \quad (2.11)$$

This quantity $K(t, r)$ vanishes outside the perturbed region so that the solution asymptotically approaches the background FLRW solution at spatial infinity.

We denote the comoving radius of a perturbed region by r_i , the precise definition of which will be given later (see eq. (2.15)), and define a dimensionless parameter ϵ in terms of the square ratio of the Hubble radius H_0^{-1} to the physical length scale of the configuration,

$$\epsilon \equiv \left(\frac{H_0^{-1}}{S(t)r_i} \right)^2 = (\dot{S}r_i)^{-2} = \frac{t_i^{2\alpha}t^\beta}{\alpha^2 r_i^2}, \quad \beta \equiv 2(1 - \alpha). \quad (2.12)$$

When we set the initial conditions for PBH formation, the size of the perturbed region is much larger than the Hubble horizon. This means $\epsilon \ll 1$ at the beginning, so it can serve as an expansion parameter to construct an analytic solution of the system of Einstein equations to describe the spatial dependence of all the above variables at the initial moment when we set the initial conditions. In this paper, the second order solution, obtained in PNY, is basically used to provide the initial conditions for the numerical computations.

We define the initial curvature profile as

$$K(0, r) \equiv K_i(r), \quad (2.13)$$

where $K_i(r)$ is an arbitrary function of r which vanishes outside the perturbed region. Note that, from (2.11), $K_i(r)$ has to satisfy the condition

$$K_i(r) < \frac{1}{r^2}. \quad (2.14)$$

We normalize radial Lagrangian coordinate r in such a way that $K_i(0) = 1$.

In order to represent the comoving length scale of the perturbed region, we use the co-moving radius, r_i , of the overdense region. We can calculate r_i by solving the following equation for the energy density perturbation defined by (2.9):

$$\delta(t, r_i) = 0. \quad (2.15)$$

Since the initial condition is taken at the superhorizon regime, when ϵ is extremely small, the following lowest-order solution[46]

$$\delta(t, r) = \frac{2r_i^2}{9r^2} (r^3 K_i(r))' \epsilon(t) \quad (2.16)$$

suffices to calculate r_i , which is obtained by solving

$$3K_i(r_i) + r_i K_i'(r_i) = 0. \quad (2.17)$$

Note that the physical length scale in the asymptotic Friedmann region is obtained by multiplying by the scale factor $S(t)$, the normalization of which we have not specified. We can therefore set up initial conditions for the PBH formation with arbitrary mass scales by adjusting the normalization of $S(t)$ which appears in the expansion parameter.

We also introduce the averaged over-density, denoted by $\bar{\delta}$ and defined as the energy density perturbation averaged over the over-dense region as follows:

$$\bar{\delta}(t) \equiv \left(\frac{4}{3} \pi R(t, r_{\text{od}}(t))^3 \right)^{-1} \int_0^{R(t, r_{\text{od}}(t))} 4\pi \delta R^2 dR. \quad (2.18)$$

Here $r_{\text{od}}(t)$ represents the comoving radius of the overdense region and is the solution of $\delta(t, r_{\text{od}}(t)) = 0$. It turns out that $r_{\text{od}}(t)$ is very close to r_i calculated from (2.17), i.e. lowest-order expansion.

Hereafter, we will always use the initial conditions obtained in this section.

III. BASIC EQUATIONS USED IN THE NUMERICAL COMPUTATIONS

The following equations were used in [53] to analyze the gravitational collapse of spherically symmetric masses:

$$\dot{U} = -a \left(4\pi R^2 \frac{\Gamma}{w} P' + \frac{MG}{R^2} + 4\pi GPR \right), \quad (3.1)$$

$$\dot{R} = aU, \quad (3.2)$$

$$\frac{(\nu R^2)'}{\nu R^2} = -a \frac{U'}{R'}, \quad (3.3)$$

$$\dot{E} = -P \left(\frac{1}{\nu} \right)', \quad (3.4)$$

$$\frac{(aw)'}{aw} = \frac{E' + P(1/\nu)'}{w}, \quad (3.5)$$

$$M = 4\pi \int_0^r \rho R^2 R' dr, \quad (3.6)$$

$$\Gamma = 4\pi \nu R^2 R', \quad (3.7)$$

$$P = \gamma \rho, \quad (3.8)$$

$$w = E + P/\nu, \quad (3.9)$$

where $E \equiv \rho/\nu$ and

$$\nu \equiv \frac{1}{4\pi b R^2}. \quad (3.10)$$

The constraint equation reads

$$\left(\frac{R'}{b} \right)^2 = \Gamma^2 = 1 + U^2 - \frac{2M}{R}. \quad (3.11)$$

We rewrite these equations in terms of the barred variables, which are defined by factoring out the scale factor S and the background energy density ρ_0 as shown below:

$$\bar{R} \equiv R/S, \quad (3.12)$$

$$\bar{a} \equiv a, \quad (3.13)$$

$$\bar{U} \equiv U/\dot{S}, \quad (3.14)$$

$$\bar{\rho} \equiv \rho/\rho_0, \quad (3.15)$$

$$\bar{M} \equiv M/(\rho_0 S^3), \quad (3.16)$$

$$\bar{b} \equiv b/S, \quad (3.17)$$

$$\bar{\nu} \equiv S^3 \nu, \quad (3.18)$$

$$\bar{\Gamma} \equiv \Gamma, \quad (3.19)$$

$$\bar{P} \equiv P/\rho_0, \quad (3.20)$$

$$\bar{w} \equiv w/(\rho_0 S^3). \quad (3.21)$$

First, using these definitions, (3.1) leads to

$$\ddot{S}\bar{U} + \dot{S}\dot{\bar{U}} = -\bar{a} \left(4\pi S^2 \bar{R}^2 \frac{\bar{\Gamma}}{S^3 \bar{w}} \bar{P}' + \frac{S \rho_0 \bar{M} G}{\bar{R}^2} + 4\pi G \rho_0 \bar{P} S \bar{R} \right). \quad (3.22)$$

Using the Friedmann equation

$$\left(\frac{\dot{S}}{S} \right)^2 = \frac{8\pi G}{3} \rho_0 \quad (3.23)$$

on the right side of (3.22) we find

$$\ddot{S}\bar{U} + \dot{S}\dot{\bar{U}} = -\bar{a} \left(4\pi S^2 \bar{R}^2 \frac{\bar{\Gamma}}{S^3 \bar{w}} \bar{P}' + \frac{3}{8\pi} \frac{\dot{S}^2}{S} \frac{\bar{M}}{\bar{R}^2} + \frac{3}{2} \frac{\dot{S}^2}{S} \bar{P} \bar{R} \right). \quad (3.24)$$

Dividing the both sides by \dot{S}^2/S and noting

$$S = \left(\frac{t}{t_i} \right)^\alpha, \quad \frac{S\ddot{S}}{\dot{S}^2} = \frac{\alpha - 1}{\alpha}, \quad (3.25)$$

we obtain

$$\frac{t}{\alpha} \dot{\bar{U}} = -\bar{a} \left(4\pi \dot{S}^{-2} \bar{R}^2 \frac{\bar{\Gamma}}{\bar{w}} \bar{P}' + \frac{3}{8\pi} \frac{\bar{M}}{\bar{R}^2} + \frac{3}{2} \bar{P} \bar{R} \right) + \frac{1 - \alpha}{\alpha} \bar{U}. \quad (3.26)$$

Defining a new time coordinate by

$$\tau \equiv \frac{\alpha}{\beta} \log \epsilon \quad (3.27)$$

and noting the following relationship

$$\frac{t}{\alpha} \frac{\partial}{\partial t} = \frac{\partial}{\partial \tau}, \quad (3.28)$$

which is obtained from the definition of ϵ , (2.12), one finds

$$(\bar{U})_\tau = -\bar{a} \left(4\pi r_i^2 \exp\left(\frac{\beta}{\alpha} \tau\right) \bar{R}^2 \frac{\bar{\Gamma}}{\bar{w}} \bar{P}' + \frac{3}{8\pi} \frac{\bar{M}}{\bar{R}^2} + \frac{3}{2} \bar{P} \bar{R} \right) + \frac{1 - \alpha}{\alpha} \bar{U}, \quad (3.29)$$

where the subscript τ denotes a time derivative with respect to τ . Similarly, (3.2)-(3.4) are rewritten in terms of the barred variables as follows:

$$\bar{R}_\tau = \bar{a} \bar{U} - \bar{R}, \quad (3.30)$$

$$\frac{(\bar{\nu} \bar{R}^2)_\tau}{\bar{\nu} \bar{R}^2} = -\bar{a} \frac{\bar{U}'}{\bar{R}'} + 1, \quad (3.31)$$

$$\bar{E}_\tau = -\bar{P} \left(\frac{1}{\bar{\nu}} \right)_\tau. \quad (3.32)$$

Since the barred variables are defined by factoring out S and ρ_0 , depending only on time, the equations (3.5)-(3.10), which do not contain time derivatives, do not change their appearance even after being rewritten in terms of the barred variables:

$$\frac{(\bar{a}\bar{w})'}{\bar{a}\bar{w}} = \frac{\bar{E}' + \bar{P}(1/\bar{\nu})'}{\bar{w}}, \quad (3.33)$$

$$\bar{M} = 4\pi \int_0^r \bar{\rho} \bar{R}^2 \bar{R}' dr, \quad (3.34)$$

$$\bar{\Gamma} = 4\pi \bar{\nu} \bar{R}^2 \bar{R}', \quad (3.35)$$

$$\bar{P} = \gamma \bar{\rho}, \quad (3.36)$$

$$\bar{w} = \bar{E} + \bar{P}/\bar{v}, \quad (3.37)$$

$$\bar{v} = \frac{1}{4\pi\bar{b}\bar{R}^2}. \quad (3.38)$$

The following equation is equivalent to (3.33) and is also useful:

$$\bar{a} = \bar{\rho}^{-\frac{\gamma}{1+\gamma}}. \quad (3.39)$$

Lastly, the constraint equation (3.11) can be rewritten as

$$\bar{\Gamma} = 1 + \dot{S}^2(\bar{U}^2 - \frac{3\bar{M}}{4\pi\bar{R}}). \quad (3.40)$$

This equation is not used for time evolution but rather is used to estimate numerical errors. Now, all the relevant equations in terms of the barred variables, (3.29), (3.30), (3.31), (3.32), (3.34), (3.35), (3.36), (3.37), (3.38), (3.39) and (3.40) have been obtained. The boundary conditions are imposed such that $\bar{U} = \bar{R} = \bar{M} = 0$ and $\bar{\Gamma} = 1$ at the centre, and $\bar{a} = \bar{\rho} = 1$ on the outer boundary so that the numerical solution is smoothly connected to the FLRW solution.

In the next section we discuss the numerical solutions of the basic equations presented here.

IV. TYPICAL TIME EVOLUTION OF PERTURBED REGIONS IN THE COSMIC TIME SLICING: A REVIEW

In order to test our numerical code which solves the evolution equations described in the previous section, we first adopt the following two-parameter family of curvature profile

$$K_i(r) = \left[1 + \frac{B}{2} \left(\frac{r}{\sigma}\right)^2\right] \exp\left[-\frac{1}{2} \left(\frac{r}{\sigma}\right)^2\right], \quad (4.1)$$

which was also investigated in [46](hereafter PM), in order to examine the consistency with the results obtained in PM. As mentioned previously, the amplitude of the profile is set to unity at the origin, meaning that we use the same normalization as a spatially closed Friedmann universe. Here the parameters B and σ control the shapes of initial perturbations. The range of B is limited to $0 \leq B \leq 1$ so that $K_i(r)$ is a monotonic function. Two examples of (4.1) are shown in Figure 1.

In order to relate the initial curvature perturbation to the amplitude of the density perturbation, following PM, let us approximately evaluate the energy density perturbation averaged over the overdense region, denoted by $\bar{\delta}$ and defined by (2.18), at the time of the horizon crossing. Using (2.16) $\bar{\delta}(t)$ becomes

$$\bar{\delta}(t) = \left(\frac{4}{3}\pi r_i^3\right)^{-1} \int_0^{r_i} \frac{8\pi r_i^2}{9} (r^3 K_i(r))' \epsilon(t) dr = \frac{2}{3} K_i(r_i) r_i^2 \epsilon(t). \quad (4.2)$$

By setting $\epsilon(t) = 1$, we define

$$\bar{\delta}_{\text{hc}} \equiv \frac{2}{3} K_i(r_i) r_i^2. \quad (4.3)$$

Note that (4.2) is valid only when $\epsilon(t) \ll 1$, so this formula gives just an approximate value of $\bar{\delta}(t)$ at the time of the horizon crossing. Still, (4.3) gives a good indicator of how strong gravity is.

A profile for which $\bar{\delta}_{\text{hc}}$ is small corresponds to a small amplitude perturbation and PBH is not formed from this kind of initial configurations. The narrow profile in Figure 1 with $(B, \sigma) = (0, 0.3)$ corresponds to $\bar{\delta}_{\text{hc}} = 0.04$, while the wide profile with $(B, \sigma) = (1, 0.7)$ corresponds to $\bar{\delta}_{\text{hc}} = 0.51$. So the width of $K_i(r)$ approximately tells how large $\bar{\delta}_{\text{hc}}$ is, as can be seen from (4.3). In the

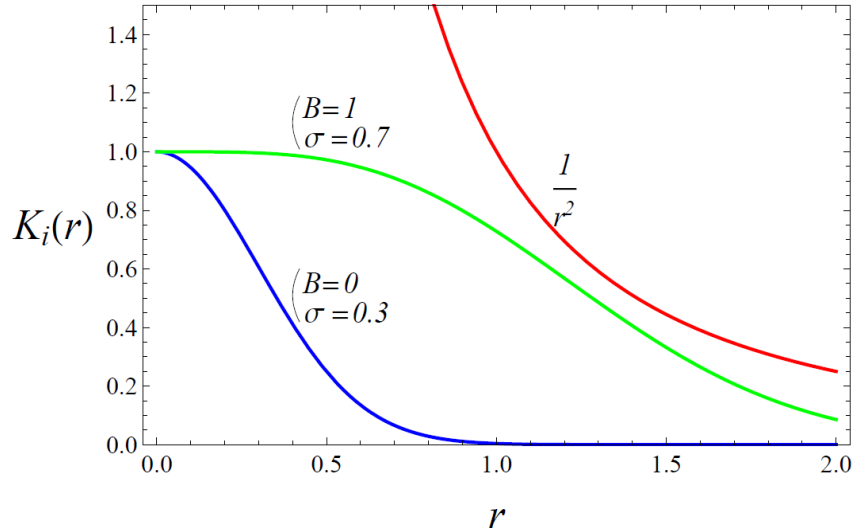


FIG. 1: A wide and narrow initial curvature profiles $K_i(r)$ represented by (4.1). Note that $K_i(r)$ has to satisfy the condition $K_i(r) < 1/r^2$.

following the time evolution of the initial perturbed region for these two cases is presented as illustration.

First, let us look at the case of the narrow profile ($\bar{\delta}_{\text{hc}} = 0.04$). The time evolution of the energy density $\bar{\rho}$, normalised by the background energy density, is shown in Figure 2. In this case the growth of the perturbation stops at some point in time after the horizon crossing and the energy density starts to decrease in the central region, with a sound wave propagating outward, the amplitude of which gradually decreases. That is, the initial perturbation dies away and the eventual state at $t = \infty$ is the flat FLRW universe.

Next, let us consider a case where the amplitude of the initial perturbation is sufficiently large ($(B, \sigma) = (1, 0.7)$, $\bar{\delta}_{\text{hc}} = 0.51$) and a PBH is eventually formed. The time evolution of $\bar{\rho}$, U and $2M/R$ in this case is shown in Figure 3.

Near the centre the energy density increases drastically and the central perturbed region gradually expands outward. The central perturbed region is always surrounded by the under-dense region.

From (2.10) U is written as $U = HR$ and it corresponds to the recession velocity in the FLRW universe. At an early stage, when the amplitude of the perturbation is small, U is positive everywhere-reflecting the expansion of the universe. In the central region where gravity becomes increasingly stronger, the expansion decelerates rapidly and therefore U decreases rapidly. Then at some point in time, the central region stops expanding and U becomes negative there, starting gravitational contraction.

The mass M is defined by (2.3) and represents the total energy contained in a sphere of radius R . When the amplitude of perturbation is small, $M \sim \rho_0(t)R(t, r)^3$ hence $2M/R \propto R^2$. As mentioned earlier, at a later stage the energy density in the central region increases dramatically as a black hole is formed, which is contrasted with the decrease in the energy density in the surrounding region due to the expansion of the universe. In such a situation the mass profile in the central

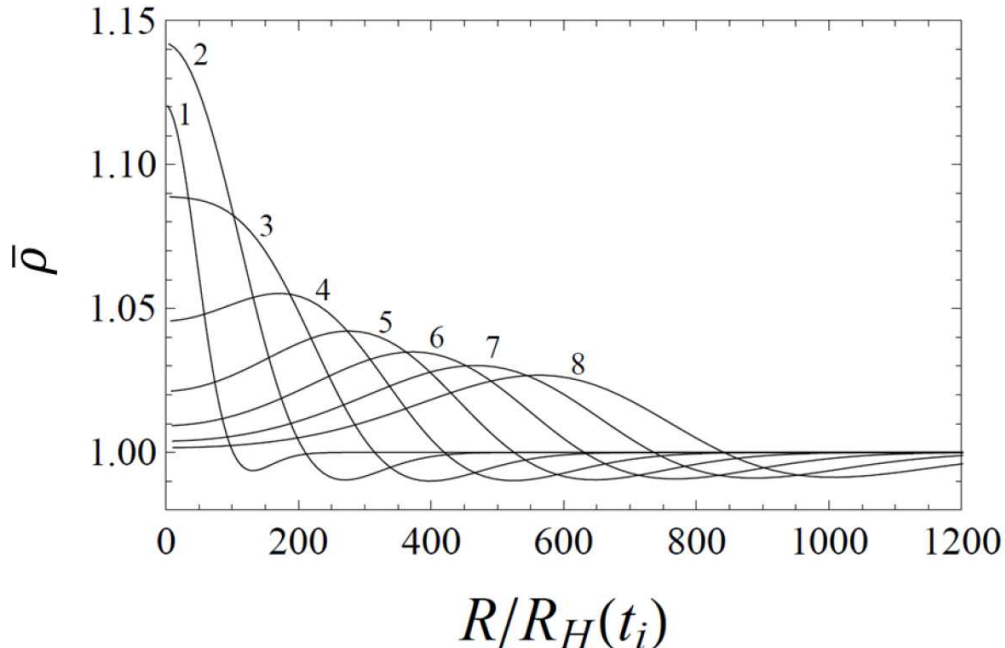


FIG. 2: An example of the time evolution of the energy density perturbation $\bar{\rho}$, normalised by the background energy density, in a case where $(B, \sigma) = (0, 0.3)$ and no PBH is formed. The plots are numbered in order of time evolution.

region is steep but is relatively gentle in the surrounding region. This feature of the mass profile can be easily understood by an analogy with a situation where a star resides in the vacuum, in which case the mass profile is a monotonically increasing function inside the radius of the star and is flat outside that radius. Due to this behaviour of M at a later stage, in the region away from the centre the mass only weakly depends on R and so approximately $2M/R \propto R^{-1}$ there. This means that a peak appears in the profile of $2M/R$ at some moment in cases where perturbation grows sufficiently. Specifically, in cases where a black hole is formed, the height of this peak exceeds unity and this implies the formation of the apparent horizon from the following arguments[54].

Suppose the trajectory of a photon moving outward, along which

$$adt = bdr, \quad (4.4)$$

so along the geodesic of this photon,

$$\frac{dR}{dt} = \frac{\partial R}{\partial t} dt + \frac{\partial R}{\partial r} dr = a(U + \Gamma)dt, \quad (4.5)$$

where the definition of U (2.2) and $\Gamma = R'/b$, followed from (3.7) and (3.10), have been used. From this we find $dR/dt = 0$ where $U = -\Gamma$ holds, meaning the photon reaching that point cannot escape further away from the centre. Since we find $U = -\Gamma$ when $2M/R = 1$ from the constraint (3.11), the peak of $2M/R$ with the height exceeding unity means that there exist photons which are trapped by the gravitational potential of the central black hole and cannot escape to infinity. Namely, the apparent horizon has been formed.

We have calculated the time evolution with various values of B and σ and obtained results fully consistent with PM. In the next section, we discuss the PBH formation condition for a much wider class of profiles than that defined by (4.1) .

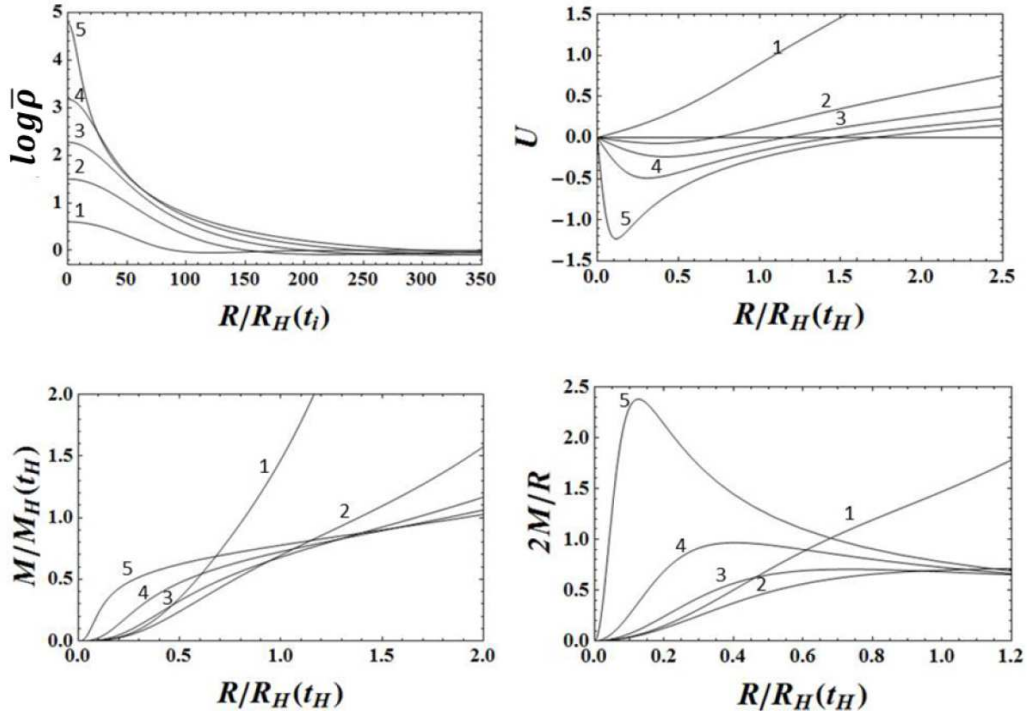


FIG. 3: Examples of time evolution of $\bar{\rho}$ (top-left), U (top-right), M (down-left) and $2M/R$ (down-right), calculated using the cosmic time slicing. These are obtained for the case $(B, \sigma) = (1, 0.7)$ and a PBH is formed. Each line is numbered in order of the time evolution.

V. TWO MASTER PARAMETERS CRUCIAL FOR PBHS FORMATION

We now proceed to our full analysis introducing the following function

$$K_i(r) = A \left[1 + B \left(\frac{r}{\sigma_1} \right)^{2n} \right] \exp \left[- \left(\frac{r}{\sigma_1} \right)^{2n} \right] + (1 - A) \exp \left[- \left(\frac{r}{\sigma_2} \right)^2 \right], \quad (5.1)$$

which can represent various shapes of profiles using the five parameters as is shown in Figure 4. Profiles with $A = 1$ include the profiles studied in PM but can also incorporate those with a steeper transition to the homogeneous region, whereas the inclusion of the second term makes it possible to further realize profiles with tails (see Figure 4). It also turned out that this function with $n = 2$ can fit the profiles investigated in [45] sufficiently well, after translating their profiles into our $K_i(r)$ since a different coordinate system was used there. Thus our function not only includes those investigated in previous work but also enables us to investigate new shapes of profiles.

For each set of five parameters, the time evolution of the perturbation is calculated to reveal whether or not a PBH is formed at the end. First, let us try to describe PBH formation condition for these various kinds of profiles using the quantity $\bar{\delta}_{\text{hc}}$ and

$$\Omega \equiv \max_r |K'_i(r)|, \quad (5.2)$$

which corresponds to Δ in PM and may provide a measure of the density gradient, or the pressure gradient for the case of the radiation-dominated universe. As can be seen in Figure 5, these two quantities fail to distinguish between the profiles which lead to PBH formation and those which

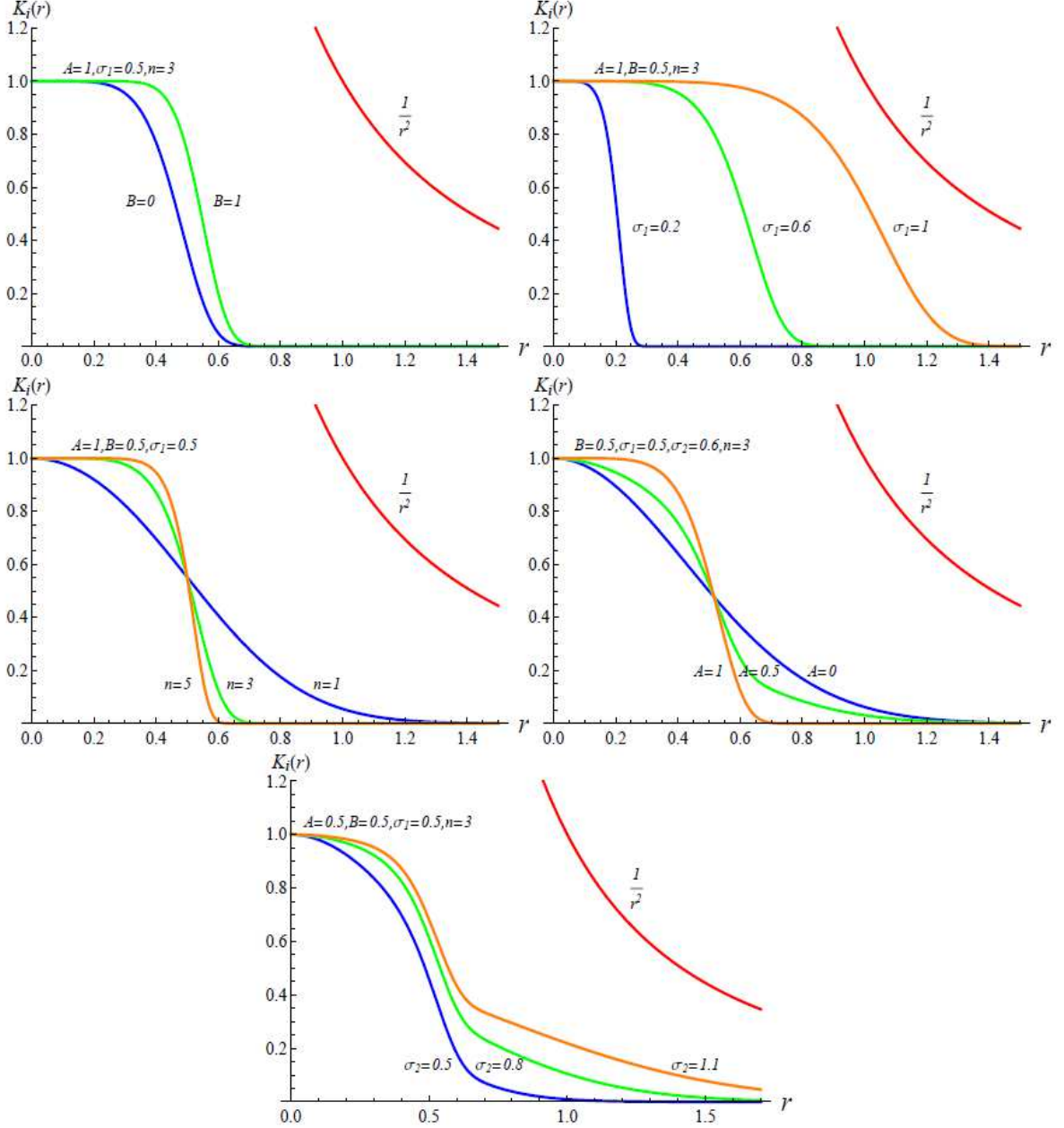


FIG. 4: Dependence of the shapes of profiles represented by (5.1) on parameters. In each panel, the dependence of the shape on one of the parameters is shown with the rest of the parameters fixed.

do not. One conceivable reason why this combination fails is because $\bar{\delta}_{\text{hc}}$ is too sensitive to the edge $r = r_i$ of configurations. To see this let us consider two profiles with almost the same shape near the centre but one of these has slightly wider tail with a larger r_i than the other. For this wider profile, $\bar{\delta}_{\text{hc}}$ is smaller since this quantity is the energy density perturbation averaged inside $r < r_i$. However, what is important in physically determining whether a PBH is formed or not is the shape of profile near the centre, while the information around the outer boundary is less

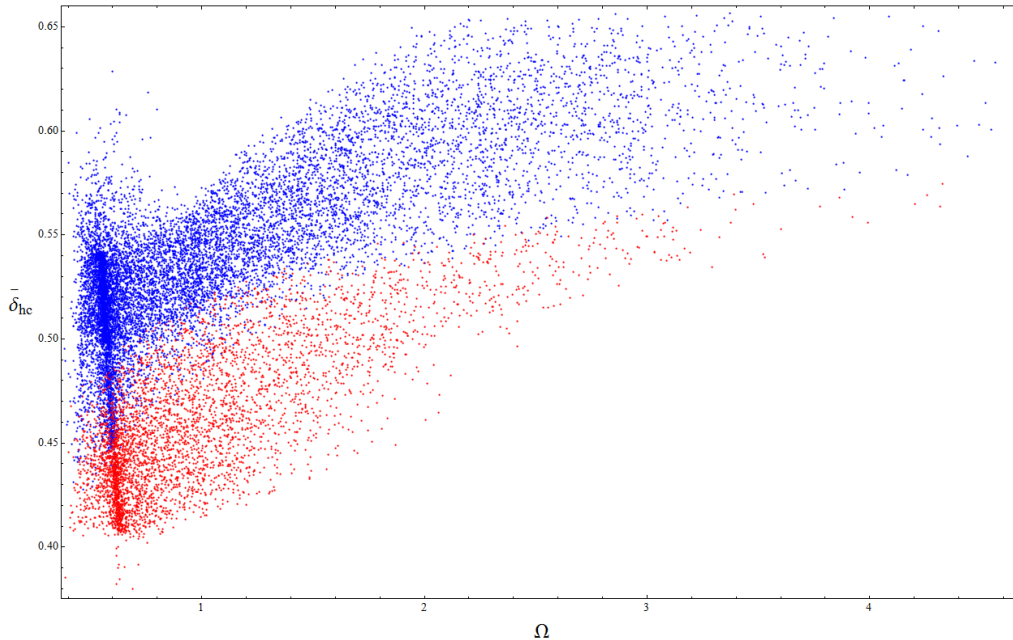


FIG. 5: The blue points correspond to profiles which lead to PBH formation and the red points to profiles which do not. Blue and red points are not well separated by a single line in this diagram.

important. Therefore, proper quantities which can clearly distinguish between the PBH-forming profiles and the non-forming ones should take the same value for those two profiles with the same shape in the centre. But $\bar{\delta}_{\text{hc}}$ takes different values for these two and as a result this fails, especially when profiles with tails are included, as depicted in Figure 5. This also shows that investigating limited types of shapes only, as has been done in the previous works, is insufficient to reveal the PBH formation condition which is generally accurately applicable to various profiles.

In order to obtain reliable measures to judge if PBHs are formed or not, we must introduce parameters which can separate the effects of the central part collapsing into holes and those of the surrounding tail part. Let us define r_p ($0 < p < 1$) by

$$K_i(r_p) = p. \quad (5.3)$$

After a number of trials of combinations

$$\Delta_{p,q} \equiv r_p - r_q, \quad (5.4)$$

$$I_{s,j} \equiv \int_0^{r_s} r^j K_i(r) dr, \quad (5.5)$$

where $p < q$ and $j = 0, 1, 2$, it turned out that a relatively clear separation between configurations which collapse to PBHs and those which do not is obtained by the following combination:

$$\Delta \equiv r_{1/6,5/6} = r_{1/6} - r_{5/6} \quad (5.6)$$

and

$$I \equiv I_{3/5,2} = \int_0^{r_{3/5}} r^2 K_i(r) dr. \quad (5.7)$$

The quantity I is similar to $\bar{\delta}_{\text{hc}}$ in the sense that it is a volume integral of curvature profile closely related to the density fluctuations (see eq. (4.2)), but the important difference is that it is not

affected by the tail part of the overdense region, since the upper limit of the integral is cut off at $r_{3/5}$. On the other hand, Δ represents the width of the transition region between $K_i \sim 1$ and $K_i \sim 0$.

Figure 6 shows the results of numerical calculation with various initial conditions of the five-parameter family (5.1). Specifically we have chosen the values of model parameters in (5.1) in the range $0 \leq A \leq 1$, $0 \leq B \leq 1$, $\sigma_{\min} \leq \sigma_1 \leq \sigma_2 \leq \min\{2\sigma_1, 1.14/\sqrt{1-A}\}$, where σ_{\min} is chosen to search only the profiles relevant to revealing the PBH formation condition and $n = 1, 2, 3, 4, 5$. The reason for the upper bound of σ_2 is because if σ_2 is too large compared to σ_1 , the second term of the function (5.1) dominates and therefore this function reduces to a single gaussian. In each numerical simulation, the values of the five parameters are chosen randomly from the range of each parameter. The initial conditions are set up by the second order asymptotic expansion. The eventual numerical errors, estimated by the constraint equation (3.40) have been confirmed to be less than a few .

As is seen there the condition for PBH formation can be quite well described by the following fitting formula:

$$(S_1(\Delta - \Delta_b) + I_b)\Theta(-(\Delta - \Delta_b)) + (S_2(\Delta - \Delta_b) + I_b)\Theta(\Delta - \Delta_b) < I, \quad (5.8)$$

where Θ denotes the unit step function and $(S_1, S_2, \Delta_b, I_b) = (-0.021, -0.32, 0.79, 0.41)$, which represent the slopes of the two lines and the position of the break. This formula corresponds to the lower solid line in Figure 6. Figure 7 depicts the initial profiles corresponding to the points A through F marked in Figure 6 to provide insights into the shapes of the profiles in each domain of the Figure 6.

Note that for the larger values of Δ , the threshold value for PBH formation I is smaller. This is because when Δ is larger, the pressure gradients are smaller and in addition gravity is relatively stronger even away from the centre, in which case gravity near the centre, measured by I , needs not be so large compared to cases with a smaller Δ . Put differently, for $I \lesssim 0.43 \equiv I_{\text{cr}}$, profiles with a smaller Δ do not result in PBH formation because the pressure gradient is so large that the gravitational collapse is hindered.

On the other hand, for $I \gtrsim I_{\text{cr}}$ the criterion is not so sensitive to Δ for the following reason. Since we are using a normalization condition $K_i(0) = 1$, the configurations with a large I must also have a large $r_{3/5}$. Thus those with $I \gtrsim I_{\text{cr}}$ have such a large $r_{3/5}$ that the difference in Δ does not affect the formation criterion much. Note that (Δ, I) can distinguish between the PBH-forming profiles and the non-forming cases much more decisively than $(\Omega, \bar{\delta}_{\text{hc}})$. This is partly because (Δ, I) does not reflect the information near the outer boundary around $r = r_i$ so much as $\bar{\delta}_{\text{hc}}$.

Some of the readers may be worried about the existence of some red points corresponding to *non*-PBH forming profiles in the BH formation region (the blue region), namely, false positives, and some blue points in the red region (false negatives). Note that it is in principle impossible to distinguish between two possibilities with 100 accuracy using only two quantities, while considering the profiles controlled by as many as five parameters. However, we argue that this choice of quantities, (Δ, I) , separates two regions fairly well with high accuracy. The false positives and the false negatives constitute only around 2.1 of all the points in Figure 6. That is, eq.(5.8) can tell whether a PBH is formed or not with around 2.1 accuracy. Note that this percentage is calculated only from the profiles appearing in Figure 6, which are randomly generated relatively near the threshold line to reveal PBH formation condition. The fitting formula was obtained by minimizing this percentage. On the other hand, the points in the gmixed regionh in Figure 5 constitute around 10 of all the points. Therefore, the accuracy would be around 10 for the case of $(\Omega, \bar{\delta}_{\text{hc}})$, if the

threshold line was drawn somehow in Figure 5, as is done in Figure 6. Note that Figures 6 and 5 are depicted with exactly the same set of 5-parameter choices.

The dashed line in Figure 6 corresponds to the Carr's condition eq.(1.1). Note that the value '1/3' was obtained in the uniform hubble slicing and this value corresponds to $\bar{\delta}_{\text{hc}} \simeq 0.22$ in the comoving slicing [60]. It turned out that the profiles for which $\bar{\delta}_{\text{hc}} \simeq 0.22$ is distributed around the dashed line in Figure 6, so the original Carr's condition roughly corresponds to $0.1 \lesssim I$.

The horizontal line in Figure 6, originating from $K_i(r) < 1/r^2$, is obtained as follows. First, note that the ideal profile which gives the maximum value of I for some Δ is $K_i(r) = 1$ ($0 < r < 1$), $1/r^2$ ($1 < r < \sqrt{6/5} + \Delta$), 0 ($\sqrt{6/5} + \Delta < r$), when $\Delta \leq \sqrt{6} - \sqrt{6/5} \simeq 1.35$. In addition, when $\sqrt{5/3} - \sqrt{6/5} \simeq 0.2 \leq \Delta$, the value of I for this ideal profile, namely, the maximum value of I for corresponding Δ , is $1/3 + \sqrt{5/3} - 1 \simeq 0.62$, hence the horizontal line.

Let us summarize this section emphasizing the key points of what has been done. What is important and new is that we have investigated various shapes of profiles altogether, including those profiles which were not investigated in the previous work as well as those investigated previously. We formed "master variables" which decide if PBHs are formed or not. This means that even though our profiles now include 5 parameters, only two master variables are important in order to determine if a PBH forms. Such a detailed analysis has never been done before. Indeed note that in the previous publications the variety of shapes was restricted, where the profiles were usually parameterized by at most two parameters. Figure 6 tells that the PBH formation condition can be simply described by using only two quantities for the whole variety of profiles, represented by 5 parameters. To reach our conclusion depicted in Figure 6, we made a lot of trials and errors to find the two master variables which we can use to clearly separate the domains of PBH formation and non-formation. So our result in Figure 6 is not merely a re-parameterization of the previously known results but goes far beyond them. We stress once again that it is important to use variables which can separate the effects of the central part and the boundary region.

In this section the time evolution of the perturbed region is calculated in the cosmic time slicing, but the problem with this slicing is that computation stops because a singularity shows up at the centre soon after the apparent horizon is formed. Thus, although this slicing serves well to determine the criteria of PBH formation, we cannot use it to investigate the final mass, which is essential in order to determine the mass spectrum. In the next section, we discuss the determination of the mass with a singularity avoided using what is called the null slicing.

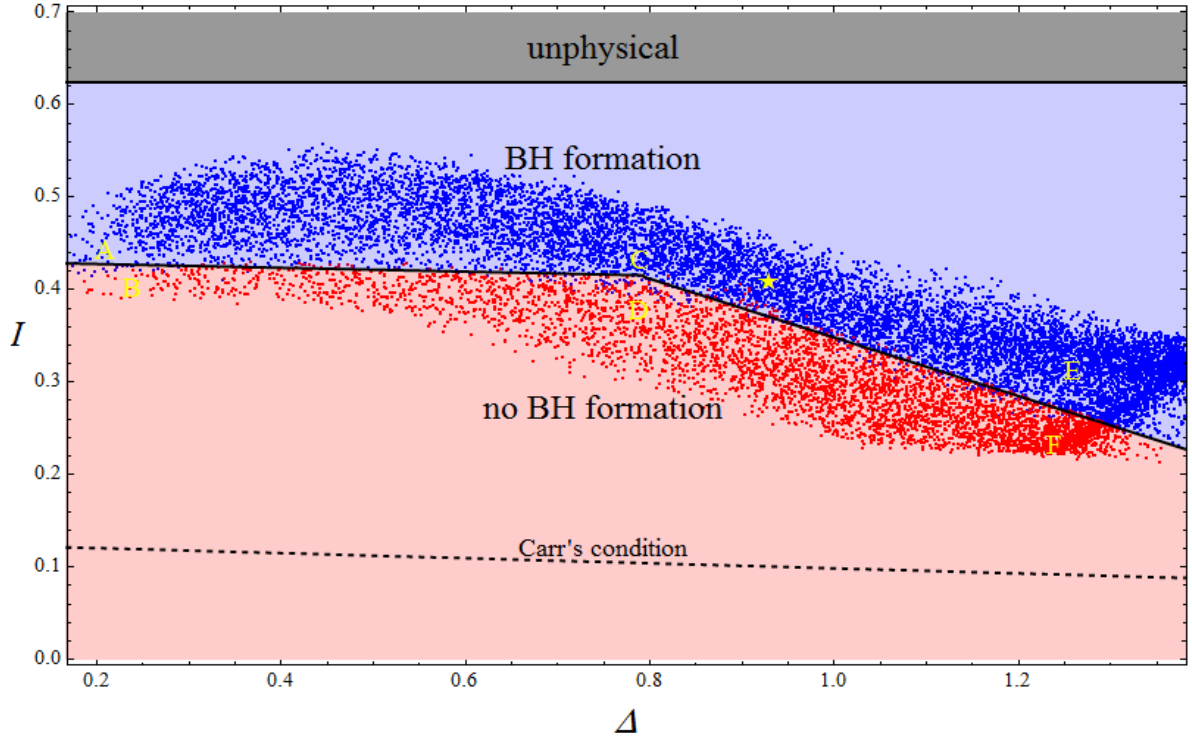


FIG. 6: The PBH formation condition for the profiles represented by (5.1). The blue and red points correspond respectively to the profiles which lead to the black hole formation and those which do not. The shaded region labelled "unphysical" corresponds to the profiles which do not satisfy $K_i(r) < 1/r^2$ and therefore are unphysical. The profile used as an example of the PBH-forming cases in this paper corresponds to the yellow star in this figure. The dashed line corresponds to the Carr's condition.

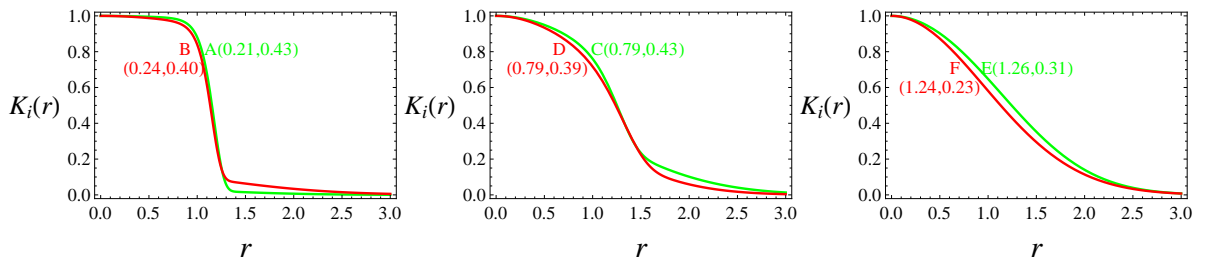


FIG. 7: Profiles corresponding to the points marked as A-F in Figure 6 with values of (Δ, I) for each profile.

VI. ACCRETION ONTO PBHS AND NULL SLICING

The determination of the mass without facing a singularity by using the null slicing [48, 55–58] is discussed in this section. In this slicing, the space-time is sliced along the null geodesics of hypothetical photons emitted from the centre and reaching a distant observer. In other words, the space-time is sliced with the hyper-surfaces, each defined by a constant null coordinate u , the so-called observer time defined shorterly. By this construction of the null slicing, only the information outside the horizon is calculated, without looking into what happens inside the apparent horizon. The initial conditions are given on some hypersurface defined by $u = \text{const.}$, which is depicted by a blue dotted line in Figure 8, and are obtained using the cosmic time slicing by calculating the null geodesic of a hypothetical photon which reaches a distant observer after being emitted from the centre at some moment in time, while at the same time recording the physical quantities of this null geodesic [57]. As is seen in Figure 8, in this slicing, the information can be obtained

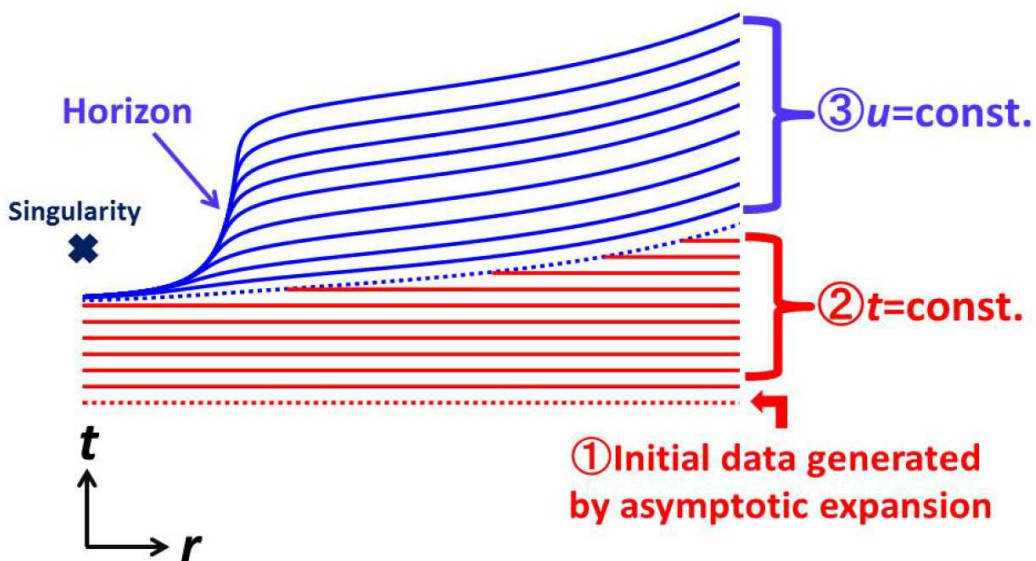


FIG. 8: Illustration of how a singularity is avoided in the null slicing.

without facing a singularity until a sufficiently later time when the eventual mass of a PBH can be determined.

Let us define the time variable u by first noting

$$adt = bdr \quad (6.1)$$

along an outgoing photon. Then, u is defined by

$$fdu = adt - bdr, \quad (6.2)$$

where f is the lapse function and is necessary to make du a perfect differential. From this definition, (6.1) holds along the hyper-surfaces each defined by $u = \text{const.}$, meaning that these surfaces correspond to the null geodesics of outgoing photons. Using u as the time variable then means that the space-time is sliced with the null slices. A boundary condition on the lapse function is imposed by setting $a(u, r = \infty) = f(u, r = \infty) = 1$, hence $u = t$ at the surface defined by $r = \infty$. The

physical meaning of this boundary condition is that u is chosen to coincide with the proper time measured by a distant observer residing at spatial infinity in the background FLRW universe. For this reason, the null slicing is also sometimes referred to as observer time slicing in the literature.

Let us look at the relationship between the derivatives in the two slicings. For the spatial derivatives, one finds from (6.2)

$$\frac{1}{b} \frac{\partial}{\partial r} \Big|_u = \frac{1}{b} \frac{\partial}{\partial r} \Big|_t + \frac{1}{a} \frac{\partial}{\partial t} \Big|_r. \quad (6.3)$$

Specifically for a function $f(t)$, depending only on t ,

$$\frac{1}{b} \frac{\partial}{\partial r} \Big|_u f(t) = \frac{1}{a} \frac{\partial}{\partial t} \Big|_r f(t). \quad (6.4)$$

For the time derivatives one immediately finds from (6.1),

$$\frac{\partial}{\partial u} \Big|_r = \frac{f}{a} \frac{\partial}{\partial t} \Big|_r. \quad (6.5)$$

The Einstein equations in the null slicing were obtained in [55] and were later used to simulate the gravitational collapse followed by the formation of a black hole [56, 57] and recently to simulate the PBH formation as well [48, 58]. We used numerical techniques similar to those used in [57, 58]. The fundamental equations are as follows:

$$U = \frac{1}{f} R_u, \quad (6.6)$$

$$\frac{1}{f} M_u = -4\pi R^2 P U, \quad (6.7)$$

$$E_u = -P \left(\frac{1}{\nu} \right)_u, \quad (6.8)$$

$$b = \frac{1}{4\pi\nu R^2}, \quad (6.9)$$

$$\frac{1}{f} U_u = -\frac{3}{2} \left(\frac{4\pi\Gamma R^2}{w} P' + \frac{M + 4\pi R^3 P}{R^2} \right) - \frac{1}{2} \left(4\pi\nu R^2 U' + \frac{2U\Gamma}{R} \right), \quad (6.10)$$

$$\frac{1}{f} \left(\frac{1}{\nu} \right)_u = \frac{1}{\nu\Gamma} \left(\frac{2U\Gamma}{R} + 4\pi\nu R^2 U' - \frac{1}{f} U_u \right), \quad (6.11)$$

$$\frac{1}{b} \left(\frac{\Gamma + U}{f} \right)' = -4\pi R \frac{\rho + P}{f}, \quad (6.12)$$

where the subscript u denotes differentiation with respect to u . Let us rewrite these equations in terms of the barred variables, defined previously. To do this, it is better to rewrite the u derivatives by the t derivatives since the barred variables were defined by factoring out $S(t)$ and $\rho_0(t)$, depending only on t . For example, using (6.5) and the definitions of the barred variables, (6.7) can be rewritten as

$$(S^3 \rho_0)' + S^3 \rho_0 \dot{\bar{M}} = -4\pi S^2 \dot{S} \rho_0 \bar{a} \bar{R}^2 \bar{P} \bar{U}, \quad (6.13)$$

so

$$\dot{\bar{M}} = -4\pi \frac{\alpha}{t} \bar{a} \bar{R}^2 \bar{P} \bar{U} - \left(\frac{3\alpha}{t} - \frac{2}{t} \right) \bar{M}, \quad (6.14)$$

which then yields

$$\bar{M}_\tau = -4\pi \bar{a} \bar{R}^2 \bar{P} \bar{U} + 3\gamma \bar{M}, \quad (6.15)$$

with the help of (2.5) and (3.28). Similarly, (6.6) leads to

$$\bar{R}_\tau = \bar{a}\bar{U} - \bar{R}, \quad (6.16)$$

and also, noting (3.28) and (6.5), (6.8) gives

$$\bar{E}_\tau = -\bar{P} \left(\frac{1}{\bar{\nu}} \right)_\tau. \quad (6.17)$$

Equation (6.9) leads to

$$\bar{b} = \frac{1}{4\pi\bar{\nu}\bar{R}^2}. \quad (6.18)$$

Using (6.4) and the definitions of the barred variables, (6.11) can be transformed to give

$$\frac{1}{\bar{a}} \left(\frac{S^3}{\bar{\nu}} \right)_\tau = \frac{S^3}{\bar{\nu}\bar{\Gamma}} \left(\frac{2\dot{S}\bar{U}\bar{\Gamma}}{S\bar{R}} + \frac{1}{\bar{a}}\dot{S}\bar{U} + \frac{\dot{S}}{S\bar{b}}\bar{U}' - \frac{1}{\bar{a}}(\dot{S}\bar{U}) \right), \quad (6.19)$$

which can be further rewritten using (6.5) as

$$(\log \bar{\nu})_\tau = 3 - \frac{2\bar{a}\bar{U}}{\bar{R}} + \frac{1}{\bar{\Gamma}} \left(-\frac{\bar{a}}{\bar{b}}\bar{U}' + \dot{S}\frac{\partial\bar{U}}{\partial\tau} \right). \quad (6.20)$$

Using (2.5), (3.23), (6.4) and (6.5), (6.10) eventually gives

$$\begin{aligned} \bar{U}_\tau = -\bar{U} \frac{\alpha - 1}{\alpha} - \frac{3}{2\bar{a}} \left[\frac{4\pi\bar{\Gamma}\bar{R}^2}{\bar{w}} \left(\frac{1}{\dot{S}^2}\bar{P}' - \frac{2}{\alpha} \frac{1}{\dot{S}} \frac{\bar{b}}{\bar{a}}\bar{P} \right) + \frac{3}{8\pi} \frac{\bar{M} + 4\pi\bar{R}^3\bar{P}}{\bar{R}^2} \right. \\ \left. + \frac{1}{3} \left(4\pi\bar{\nu}\bar{R}^2 \left(\frac{\bar{b}}{\bar{a}} \frac{\alpha - 1}{\alpha} \bar{U} + \frac{1}{\dot{S}}\bar{U}' \right) + 2\frac{1}{\dot{S}} \frac{\bar{U}\bar{\Gamma}}{\bar{R}} \right) \right]. \end{aligned} \quad (6.21)$$

From the definitions of the barred variables and the Friedmann equation (3.23), (6.12) can be rewritten as

$$\left(\frac{\bar{\Gamma} + \dot{S}\bar{U}}{f} \right)' = -\frac{3}{2}\dot{S}^2\bar{b}\bar{R}\frac{\bar{\rho} + \bar{P}}{f}. \quad (6.22)$$

The equations in terms of the barred variables shown above include \dot{S} , which can be calculated by $\dot{S} = 1/\sqrt{\epsilon r_i^2}$, the relation obtained from (2.12). Observe that t , the time variable in the cosmic time slicing, depends on both u and r ($t = t(u, r)$) in the null slicing, so do ϵ and τ . Then it is necessary to determine ϵ and τ at a point (u, r) . To this end, note that on the surface $r = \text{const.}$, we find

$$dt(u, r) = \frac{f(u, r)}{a(u, r)} du = \frac{f(u, r)}{a(u, r)} dt(u, r = \infty), \quad (6.23)$$

which can be rewritten as

$$d\tau(u, r) = \frac{f(u, r)}{a(u, r)} \left(\frac{\epsilon(u, r = \infty)}{\epsilon(u, r)} \right)^{1/\beta} d\tau(u, r = \infty). \quad (6.24)$$

Here the definition of ϵ (2.12) and that of τ (3.27) have been used. The time step $d\tau(u, r = \infty)$ needs to be chosen to satisfy the CFL condition (see the Appendix), and the general $d\tau(u, r)$ can be calculated from (6.24).

The boundary conditions are imposed the same as in the cosmic time slicing by setting $\bar{u} = \bar{R} = \bar{M} = 0, \Gamma = 1$ at the centre and $\bar{a} = \bar{\rho} = 1$ on the outer boundary so that the numerical solution coincides with the background FLRW solution there.

We now present results of numerical computations using the null slicing. The hypersurfaces of $u = \text{const.}$, corresponding to null geodesics, are shown in the top left panel of Figure 9. Observe

that the intervals between the null geodesics are tiny in the central region, meaning that time does not pass there in effect. Therefore, the formation of a singularity can be avoided in this slicing as expected. The upper lines in this figure correspond to the null geodesics of the hypothetical photons which are emitted from the centre at later times and feel the effects of stronger gravity, so that they need more time to reach a distant observer. In this figure there is an envelope curve of the null geodesics, which shows approximately the location of the apparent horizon. In this way the time evolution is computed only outside the apparent horizon, so the eventual mass of a PBH can be determined without facing a singularity. From the same figure, the apparent horizon radius can be confirmed to asymptote to a constant value after its formation. This means that the black hole mass asymptotes to a constant value because $R = 2M$ on the apparent horizon, and this behavior of the mass can be confirmed by the converging curves of the mass profile in the bottom left panel of Figure 9.

The flatness of the mass profile in later time can be understood by noting that the energy density in a region away from the centre decreases due to the expansion of the universe and also due to the existence of an underdense region surrounding the central overdense region. As mentioned earlier, this behaviour of the mass profile is similar to that of the vacuum inhabited by a star at the centre, in which case the mass profile is a monotonically increasing function in r inside the star and is flat outside.

The time evolution of $2M/R$ is shown in the bottom right panel of Figure 9. The fact that the height of the peak of $2M/R$ saturates to unity in a late time in the null slicing is clearly seen, which is contrasted with the cosmic time slicing in which the peak is confirmed to exceed unity (see Figure 3). This feature of the time evolution being frozen near the centre in the null slicing can also be confirmed by the behaviour of the lapse function, which is shown in the top right panel of Figure 9. Note also that the spatial derivatives of f become large near the apparent horizon, which shows the necessity of Adaptive-Mesh-Refinement(AMR), described in the Appendix. Thus Figure 9 as a whole shows that using the null slicing the Einstein equations can be solved until a sufficiently late time when the eventual mass of a PBH can be determined.

In this paper the mass of a PBH for one particular profile was shown just to illustrate how the mass can be obtained by null slicing. In our future work, as was mentioned in the Introduction, we will investigate the mass evolution and the eventual mass of PBHs for a wide variety of profiles considered in this paper.

VII. CONCLUSION

In this paper we have presented the results of numerical computations of the time evolution of a perturbed region after the horizon re-entry. The initial conditions for these numerical computations were given using an analytical asymptotic expansion technique developed in our previous paper. By calculating the time evolution of various initial perturbations, the condition for PBH formation has been investigated. We have extended preceding analyses by performing many more numerical computations of PBH formation based on the initial curvature profiles characterized by five parameters which not only reproduce the variety of profiles near the centre but also incorporate the possible extended features in the tail region (see eq.(5.1)).

We have shown that the criterion of PBHs formation can still be expressed in terms of two crucial (master) parameters which correspond to the averaged amplitude of over density in the central region and the width of transition region at outer boundary. As is shown in Figure 6, this

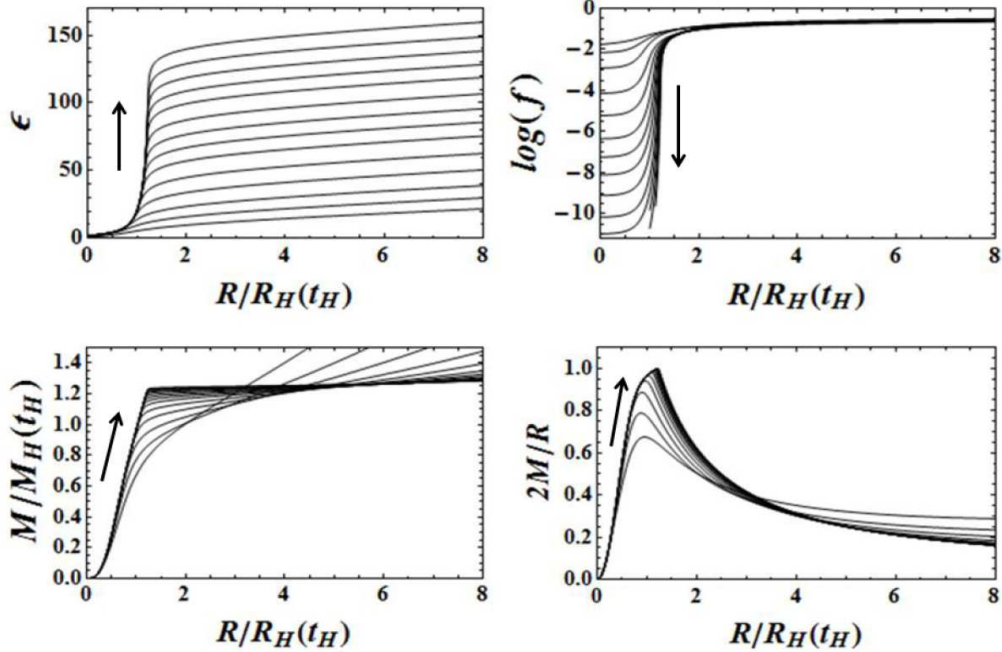


FIG. 9: Examples of time evolutions of the relevant quantities in the null slicing for the case where $(B, \sigma) = (1, 0.7)$. The horizontal line represents the circumferential radius R , normalized by the Hubble radius at the horizon crossing. The $u = \text{const.}$ surfaces are shown in the top left panel. Shown in the top right panel is the lapse function, which goes to zero near the centre. The mass M normalized by the horizon mass at the time of the horizon crossing is shown in the down left panel. The profile of $2M/R$, the height of which asymptotes to unity, is shown in the down right panel. Arrows in each figure indicate the evolution in time sequence.

is the case even though our profiles are characterized by as many as five parameters. We have also provided a reliable physical interpretation of the two-parametric criterion.

Using a null slicing we have calculated the variation of PBH mass as a result of accretion. In this paper we present only one example corresponding to $K_i(r)$ given in Figure 9. For this example, the eventual mass of the PBH is approximately equal to the horizon mass at the time of horizon crossing. The initial configuration in this example lies at the point marked by the yellow star in Figure 6, which is fairly far from the critical line. However, it has been shown that the eventual mass of a PBH can be much smaller when $\bar{\delta}_{\text{hc}}$ is extremely close to δ_{min} , the minimum value required to create a black hole [48, 59], which would fall on the critical line in Figure 6. In our future work we will explore this issue for the various types of $K_i(r)$ investigated in this paper.

Note that PBHs are formed only from extremely high peaks of perturbation, corresponding to the tail of the probability distribution of primordial perturbation. The profiles corresponding to these peaks have been calculated [50, 51] and turned out to be approximately spherically symmetric and monotonic near the peak. So in this paper we have considered only the spherically symmetric profiles which are monotonic near the centre. However, deviation from sphericity to some extent is expected so we will explore effects of non-sphericity in our future work as well.

ACKNOWLEDGMENTS

This work was partially supported by JSPS Grant-in-Aid for Scientific Research 23340058 (J.Y.), Grant-in-Aid for Scientific Research on Innovative Areas No. 21111006 (J.Y.), Grant-in-Aid for Exploratory Research No. 23654082(T.H.), and Grant-in-Aid for JSPS Fellow No. 25.8199 (T.N.). TN thanks School of Physics and Astronomy, Queen Mary College, University of London for hospitality received during this work. We thank B. J. Carr for useful communications. TN acknowledges H. Kodama, K. Kohri, K. Ioka and H. Takami for helpful comments.

Appendix

In this Appendix, a few details of the techniques used in the numerical computation of this paper are discussed.

A. Determination of time steps satisfying Courant-Friedrichs-Lewy condition

In order to guarantee numerical stability, the following Courant-Friedrichs-Lewy condition (CFL condition) has to be maintained during the entire computation:

$$c_s < \frac{\Delta r}{\Delta t}, \quad (7.1)$$

where c_s is the sound velocity, which is $1/\sqrt{3}$ during the radiation-domination, and Δr and Δt represent intervals of gridpoints and timesteps respectively. In general relativity, this CFL condition is modified as follows:

$$c_s < \frac{b(t, r)\Delta r}{a(t, r)\Delta t}, \quad (7.2)$$

which is rewritten in terms of the quantities introduced previously as

$$\Delta\tau < \frac{2\sqrt{3}(1-\alpha)\bar{b}(t, r)}{\beta r_i \sqrt{\epsilon}\bar{a}(t, r)} \Delta r. \quad (7.3)$$

In the null slicing (7.2) is rewritten to be

$$c_s < \frac{b(u, r)\Delta r}{f(u, r)\Delta u + b(u, r)\Delta r}. \quad (7.4)$$

This equation gives a condition for the time interval

$$\Delta u < \frac{1 - c_s}{c_s} \frac{b(u, r)}{f(u, r)} \Delta r, \quad (7.5)$$

which can be reexpressed noting $\Delta u = \Delta t(u, r = \infty)$ and (3.28) as a condition for $\Delta\tau(u, r = \infty)$:

$$\Delta\tau(u, r = \infty) < \frac{2(\sqrt{3}-1)(1-\alpha)}{\beta r_i} \frac{\bar{b}(u, r)}{f(u, r)\sqrt{\epsilon(u, r = \infty)}} \Delta r. \quad (7.6)$$

The time step $\Delta\tau(u, r = \infty)$ has to be chosen to satisfy this condition and general $\Delta\tau(u, r)$ can be calculated from (6.24).

B. Numerical techniques employed in the calculation in the null slicing

The following three numerical techniques are employed to minimize the amount of calculations while maintaining accuracy.

The first one is to stop computing the time evolution in the central region where time is frozen. As we have seen, $f \rightarrow 0$ (meaning $d\tau \rightarrow 0$ from (6.24)) near the centre, in the cases where a black hole is formed. So time stops in the central region, in which case the time evolution does not need to be followed solving the differential equations there.

The second technique is to choose the location of the outer boundary optimally during computation. Mathematically, the boundary conditions are imposed so that the solution coincides exactly with the background FLRW solution at spatial infinity, but in numerical computation the boundary is placed at some finite radius. The location of the outer boundary has to be chosen to be sufficiently far from the centre so that the numerical solution of the Einstein equations is sufficiently close to the solution of the FLRW universe since otherwise errors accumulate at the outer boundary and numerical computation breaks down. Suppose at some time u_1 the outer boundary is placed at $r = r_b(u_1)$, where the following inequality is satisfied:

$$|\bar{\rho}(u_1, r) - 1| < c_1, \quad (7.7)$$

with c_1 being a constant which is sufficiently small (say, 10^{-6}). Here, it is important to note that the central perturbed region gradually expands outward, as is shown in Figure 3 for example. As a result, at a later time $u_2 (> u_1)$, $r_b(u_1) < r_b(u_2)$ so (7.7) would not hold at u_2 if we took $r_b = r_b(u_1)$. If on the other hand r_b is fixed to be $r_b(u_f)$, where u_f is the final time of the numerical computation, (7.7) always holds during the computation. However, this choice leads to an unnecessarily large amount of calculations. This situation can be ameliorated by changing r_b optimally by taking the following procedures. Suppose (7.7) is satisfied at u_1 so r_b is chosen to be $r_b = r_b(u_1)$ and later (7.7) breaks at u_2 . Then, at this moment r_b is redefined to be $r_b = r_b(u_2)$ and the numerical solution in the region $r_b(u_1) < r < r_b(u_2)$ is approximated by the background FLRW solution and appended to the solution in the region $r < r_b(u_1)$, already calculated numerically. After u_2 , the differential equations are solved in the region $r < r_b(u_2)$. And if (7.7) breaks again at $u = u_3$, r_b is redefined to be $r_b = r_b(u_3)$ and the solution is approximated by the background solution in the region $r_b(u_2) < r < r_b(u_3)$, which is then appended to the numerical solution in the region $r < r_b(u_2)$. This procedure is repeated if necessary, which guarantees (7.7) during the entire computation and as a result enables a computation with a minimal number of grids while maintaining accuracy in the region far from the centre .

The third technique is the reduction of grid intervals in the region where the spatial derivatives become large, a technique known as Adaptive-Mesh-Refinement (AMR). As the perturbation grows, spatial derivatives of physical quantities become large in the central region, which can be confirmed from the top right panel of Figure 9 for instance. In order to maintain accuracy in such a situation, the grid intervals need to be reduced but doing so globally would drastically increase the number of grid points. Therefore, it is optimal to reduce the grid intervals in the central region only where the spatial derivatives become large, while the grid intervals in the region away from the centre are kept relatively large, since the spatial derivatives are modest there.

[1] Y. B. Zel'dovich and I. D. Novikov, *Sov. Astron.* **10**, 602 (1967).

- [2] S. Hawking, Mon. Not. Roy. Astron. Soc. **152**, 75 (1971).
- [3] S. Hawking, Nature **248**, 30 (1974).
- [4] Y. B. Zel'dovich, A. A. Starobinskii, M. Y. Khlopov, and V. M. Chechetkin, Sov. Astron. Lett. **3**, 110 (1977).
- [5] I. D. Novikov, A. G. Polnarev, A. A. Starobinskii, and Y. B. Zel'dovich, Astron. Astrophys. **80**, 104 (1979).
- [6] B. V. Vainer and P. D. Naselskii, Astron. Zh. **55**, 231 (1978), [Sov. Astron. **22**, 138 (1978).].
- [7] B. V. Vainer, O. V. Dryzhakova, and P. D. Naselskii, Pis ma Astronomicheskii Zhurnal **4**, 344 (1978), [Sov. Astron. Lett. **4**, 185 (1978).].
- [8] S. Miyama and K. Sato, Prog. Theor. Phys. **59**, 1012 (1978).
- [9] K. Kohri and J. Yokoyama, Phys. Rev. D **61**, 023501 (2000), astro-ph/9908160.
- [10] D. N. Page and S. Hawking, Astrophys. J. **206**, 1 (1976).
- [11] J. H. MacGibbon, Nature **329**, 308 (1987).
- [12] J. H. MacGibbon and B. J. Carr, Astrophys. J. **371**, 447 (1991).
- [13] B. J. Carr, Astrophys. J. **206**, 8 (1976).
- [14] B. Paczynski, Astrophys. J. **304**, 1 (1986).
- [15] R. Saito and J. Yokoyama, Phys. Rev. Lett. **102**, 161101 (2009), [**107**, 069901(E) (2011).], 0812.4339.
- [16] R. Saito and J. Yokoyama, Prog. Theor. Phys. **123**, 867 (2010), [**126**, 351(E) (2011).], 0912.5317.
- [17] B. Carr, K. Kohri, Y. Sendouda, and J. Yokoyama, Phys. Rev. D **81**, 104019 (2010), 0912.5297.
- [18] K. Griest, A. M. Cieplak, and M. J. Lehner (2013), 1307.5798.
- [19] A. G. Polnarev, in *Morphological Cosmology*, edited by P. Flin and H. W. Duerbeck (1989), vol. 332 of *Lecture Notes in Physics*, Berlin Springer Verlag, pp. 369–376.
- [20] K. Sato, Mon. Not. Roy. Astron. Soc. **195**, 467 (1981).
- [21] A. H. Guth, Phys. Rev. D **23**, 347 (1981).
- [22] A. A. Starobinsky, Phys. Lett. B **91**, 99 (1980).
- [23] V. F. Mukhanov and G. Chibisov, Sov. Phys. JETP **56**, 258 (1982).
- [24] A. H. Guth and S. Pi, Phys. Rev. Lett. **49**, 1110 (1982).
- [25] S. Hawking, Phys. Lett. B **115**, 295 (1982), revised version.
- [26] A. A. Starobinsky, Phys. Lett. B **117**, 175 (1982).
- [27] G. Hinshaw et al. (WMAP Collaboration) (2012), 1212.5226.
- [28] P. Ade et al. (Planck Collaboration) (2013), 1303.5082.
- [29] J. Garcia-Bellido, A. Linde, and D. Wands, Phys. Rev. D **54**, 6040 (1996).
- [30] H. M. Hodges and G. R. Blumenthal, Phys. Rev. D **42**, 3329 (1990).
- [31] P. Ivanov, P. Naselsky, and I. Novikov, Phys. Rev. D **50**, 7173 (1994).
- [32] J. Yokoyama, Astron. Astrophys. **318:673** (1997).
- [33] J. Yokoyama, Phys. Rev. D **58**, 083510 (1998).
- [34] J. Yokoyama, Phys. Rep. **307**, 133 (1998).
- [35] M. Kawasaki and T. Yanagida, Phys. Rev. D **59**, 043512 (1999).
- [36] J. Yokoyama, Prog. Theor. Phys. Suppl. **136**, 338 (1999).
- [37] R. Saito, J. Yokoyama, and R. Nagata, J. Cosmol. Astropart. Phys. **2008**, 024 (2008).
- [38] A. Taruya, Phys. Rev. D **59**, 103505 (1999).
- [39] B. A. Bassett and S. Tsujikawa, Phys. Rev. D **63**, 123503 (2001).
- [40] A. M. Green and K. A. Malik, Phys. Rev. D **64**, 021301 (2001).
- [41] M. Kawasaki, T. Takayama, M. Yamaguchi, and J. Yokoyama, Mod. Phys. Lett. **A22**, 1911

- (2007).
- [42] T. Kawaguchi, M. Kawasaki, T. Takayama, M. Yamaguchi, and J. Yokoyama, *Mon. Not. Roy. Astron. Soc.* **388**, 1426 (2008), 0711.3886.
 - [43] B. J. Carr and S. Hawking, *Mon. Not. Roy. Astron. Soc.* **168**, 399 (1974).
 - [44] B. J. Carr, *Astrophys. J.* **201**, 1 (1975).
 - [45] M. Shibata and M. Sasaki, *Phys. Rev. D* **60**, 084002 (1999), gr-qc/9905064.
 - [46] A. G. Polnarev and I. Musco, *Class. Quant. Grav.* **24**, 1405 (2007), gr-qc/0605122.
 - [47] D. K. Nadezhin, I. D. Novikov, and A. G. Polnarev, NASA STI/Recon Technical Report N **80**, 10983 (1979).
 - [48] J. C. Niemeyer and K. Jedamzik, *Phys. Rev. D* **59**, 124013 (1999), URL <http://link.aps.org/doi/10.1103/PhysRevD.59.124013>.
 - [49] A. Polnarev, T. Nakama, and J. Yokoyama, *J. Cosmol. Astropart. Phys.* **2012**, 027 (2012), URL <http://stacks.iop.org/1475-7516/2012/i=09/a=027>.
 - [50] A. Doroshkevich, *Astrophysics* **6**, 320 (1970), ISSN 0571-7256, URL <http://dx.doi.org/10.1007/BF01001625>.
 - [51] J. M. Bardeen, J. Bond, N. Kaiser, and A. Szalay, *Astrophys. J.* **304**, 15 (1986).
 - [52] C. W. Misner and D. H. Sharp, *Phys. Rev.* **136**, B571 (1964).
 - [53] M. M. May and R. H. White, Academic Press, New York and London (1967).
 - [54] I. Musco and J. C. Miller, arXiv:1201.2379 [gr-qc] (2012).
 - [55] W. C. Hernandez, Jr. and C. W. Misner, *Astrophys. J.* **143**, 452 (1966).
 - [56] J. C. Miller and S. Motta, *Class. Quant. Grav.* **6**, 185 (1989), URL <http://stacks.iop.org/0264-9381/6/i=2/a=012>.
 - [57] T. W. Baumgarte, S. L. Shapiro, and S. A. Teukolsky, *Astrophys. J.* **443**, 717 (1995).
 - [58] I. Musco, J. C. Miller, and L. Rezzolla, *Class. Quant. Grav.* **22**, 1405 (2005), URL <http://stacks.iop.org/0264-9381/22/i=7/a=013>.
 - [59] I. Musco, J. C. Miller, and A. G. Polnarev, *Class. Quant. Grav.* **26**, 235001 (2009), 0811.1452.
 - [60] T. Harada, C.-M. Yoo, and K. Kohri (2013), 1309.4201.